**Noname manuscript No.**
(will be inserted by the editor)

# COSMO: Measuring CMB spectral distortions from Antarctica

**L. Mele** [1,2] · **E.S.Battistelli** [1,2] · **P. de Bernardis** [1,2] · **M. Bersanelli**[3,4] · **F. Columbro**[1,2] · **G. Coppi**[5] · **A. Coppolecchia**[1,2] · **G. D'Alessandro**[1,2] · **M. De Petris**[1,2] · **C. Franceschet**[3,4] · **M. Gervasi**[5,6] · **L. Lamagna**[1,2] · **A. Limonta**[5,6] · **E. Manzan**[3] · **E. Marchitelli** [1] · **S. Masi**[1,2] · **A. Mennella**[3,4] · **F. Nati**[5] · **A. Paiella**[1,2] · **G. Pettinari**[7] · **F. Piacentini**[1,2] · **L. Piccirillo**[8] · **G. Pisano**[1] · **S. Realini**[3,4] · **C. Tucker**[9] · **M. Zannoni**[5,6]

the date of receipt and acceptance should be inserted later

Received: date / Accepted: date

**Abstract** COSMO is a ground-based instrument to measure the spectral distortions (SD) of the Cosmic Microwave Background (CMB). In this paper we present preliminary results of electromagnetic simulations of its reference blackbody calibrator. *HFSS* simulations provide a calibrator residual reflection coefficient of $R \sim 10^{-6}$, corresponding to an emissivity $\epsilon = 1 - R = 0.999999$. We use ILC based simulations to provide the performance forecast of the instrument. We show that COSMO can extract the isotropic comptonization parameter (assumed to be $y = 1.77 \cdot 10^{-6}$) as $|y| = (1.79 \pm 0.19) \cdot 10^{-6}$, in

L. Mele
Piazzale Aldo Moro 5
E-mail: lorenzo.mele@roma1.infn.it
[1] Università di Roma - La Sapienza, Roma, Italy
[2] INFN sezione di Roma, 00185 Roma, Italy
[3] Università degli studi di Milano, Milano, Italy
[4] INFN sezione di Milano, 20133 Milano, Italy
[5] Università di Milano - Bicocca, Milano, Italy
[6] INFN sezione di Milano - Bicocca, 20126 Milano, Italy
[7] Istituto di fotonica e nanotecnologie, Consiglio Nazionale delle Ricerche IFN-CNR, 00156 Roma, Italy
[8] Jodrell Bank Centre for Astrophysics, School of Physics and Astronomy, University of Manchester, Manchester, UK
[9] School of Physics and Astronomy, Cardiff University, Queens Buildings, The Parade, Cardiff, CF243AA, UK

the presence of the main Galactic foreground (thermal dust) and of CMB anisotropies, and assuming perfect atmospheric emission removal.

**Keywords** Cosmology · Spectral Distortions · Blackbody

## 1 Introduction

COSMO (COSmic Monopole Observer) is a ground-based cryogenic differential Fourier transform spectrometer (DFTS) which aims at measuring the isotropic $y$-distortion of the Cosmic Microwave Background (CMB). Deviations from the almost-perfect blackbody spectrum are expected in the CMB and encode information on a wide variety of processes along the thermal history of the Universe, implying energy exchanges with CMB photons. These are both processes included in the standard $\Lambda CDM$ model and ultra-high energy processes in the early Universe. Thus the measurement of SDs represents a unique way of probing new physics [1]. To date no isotropic SD have been detected at mm wavelengths and the upper limit for $y$ is still $< 1.5 \cdot 10^{-5}$ [2,3]. A cryogenic DFTS is ideally suited for CMB SD measurements, allowing for good control over systematic effects, and providing high common-mode rejection, $CMRR > 50\,\mathrm{dB}$ [4]. COSMO will be operated at Dome-C, Antarctica, one of the best sites on Earth for CMB measurements due to the level of atmospheric stability [5].

## 2 Instrument

COSMO is a cryogenic DFTS. The cryostat consists in three main stages: the vacuum shell and the 40 K and 3 K stages, cooled down by two double-stage pulse tubes. The DFTS is mounted on the 3 K stage. One of the input ports of the DFTS faces the sky through a 220 mm diameter polyethylene window and a set of thermal filters limiting the thermal load. The other input port looks at a cryogenic blackbody calibrator. This is used as a reference and features low residual reflectance ($< 10^{-6}$), corresponding to an emissivity close to unity $\epsilon = 1 - 10^{-6} = 0.999999$. The DFTS is a traditional Martin-Puplett [6] completed by three lenses, L1 and L2 in Fig.1 made of polyethylene, and L3 made of alumina. The two focal planes are equipped with multi-mode Kinetic Inductance Detectors (KIDs), 9 pixels for each array, sensitive in the 150 and 220 GHz frequency bands, matching two high-transmission atmospheric windows. The focal planes are cooled down at 250 mK via a dilution refrigerator and the expected noise-equivalent-power (NEP) and time constant ($\tau$) are NEP$\sim 3.8 \cdot 10^{-17}\mathrm{W}/\sqrt{\mathrm{Hz}}$ and $\tau \sim 60\,\mu\mathrm{s}$. The interference is modulated by moving the DFTS roof-mirror via a voice coil actuator, which provides smooth and fast motion with almost no friction, minimizing the heat load on the 3 K stage. The atmospheric emission, with its fluctuations, is measured and removed by performing fast sky-dips using a spinning wedge mirror as the first optical train element. The 5° wedge mirror, 600 mm in diameter, adds ±10° to

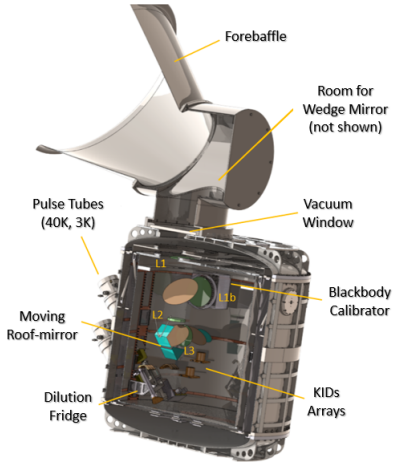


**Fig. 1** Render of the COSMO instrument.

the central elevation, rotating at 2500 rpm and collecting almost simultaneous data at different air masses within each 5 s long interferogram. Proper data binning provides interferograms, and spectra, at different elevations.

## 2.1 Blackbody Calibrator

A calibrator close to a perfect blackbody is needed for CMB SD measurements, to avoid spurious distortion signals. Assuming to perform a noise-free differential measurement of the CMB and the $y$-distortion, comparing to a calibrator at the same temperature as the CMB and with an emissivity $\epsilon$, a distortion signal arises as soon as the calibrator emissivity is $\epsilon < 1 - 10^{-6}$. In Fig. 2-(left) we report the distortion signal produced by a non-ideal blackbody calibrator: the spurious signal becomes sub-dominant for emissivity $\epsilon \geq 1 - 10^{-6}$.

Typical blackbody cavities are composed of an external metal structure which guarantees good heat exchange with the reference thermostat, and of an internal coating of absorbing material. The blackbody calibrator developed for COSMO is a single cone cavity deformed along a parabolic line, providing the absorption of input radiation through a large number of interactions ($N > 6$) with the absorbing coating, and also limiting the diffraction produced by the apex of the cavity, whose size in its final section becomes comparable to the wavelength of the incident radiation. The calibrator has a 220 mm aperture diameter and is 680 mm long. The external body will be made of copper and the absorbing coating will be a 10 mm thick layer of Eccosorb CR-110 (Emerson & Cuming), whose thermal and electromagnetic properties are well studied [7]. The thermal performance is still under optimization, however this design guarantees low thermal gradients given the material selected for the external body and thanks to several links which will thermally connect the cavity to the reference thermostat.

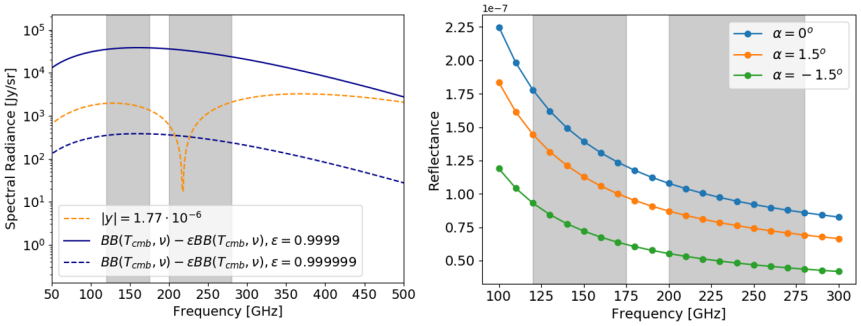


**Fig. 2** Left panel: residual produced by a non-ideal blackbody cavity in a differential measurement of CMB isotropic $y$ distortion; the bias becomes sub-dominant as the emissivity approaches $\epsilon = 0.999999$. Right panel: residual cavity reflectance estimated for different incidence angles $\alpha$ at the cavity aperture, in the ray-tracing approximation, assuming a reflection coefficient of the cavity coating from [8]. The COSMO frequency bands are shaded in gray in the plot.

The *Optics-Studio ZEMAX* software provides the performance in the geometrical optics approximation by counting the number of reflections of the input light against the cavity walls, assuming the reflectance properties of the CR110 coating as in [8], $r(\bar{\nu}) = 0.08 + \frac{0.06[cm^{-1}]}{\bar{\nu}}$, where $\bar{\nu}$ is the wavenumber. Input light rays undergo $N > 6$ reflections with the coating, corresponding to a residual reflectance $R < 10^{-6}$ over the band 100-300 GHz, guaranteeing an emissivity $1 - R$. The estimated reflectance of the cavity is reported at different incidence angles $\alpha$ in Fig.2-right, within the DFTS *F.O.V.* $= 1.5°$, and provides an emissivity $\epsilon > 0.999999$. The rays trajectories are reported in Fig.3-left.

The cavity performance has been also assessed via *HFSS* electromagnetic simulations. Given the size of the calibrator and the frequencies to be explored, only a few wavelengths thick slice of the calibrator, scaled by a factor of 3, has been included in the simulation. As a result, the simulation is representative in terms of the absorbing properties of the cavity, but is not representative of the direction of the damped outgoing radiation. The simulations have been run only for the lower frequency of the 150 GHz band. The dielectric properties of the coating at 120 GHz are relative permittivity $\epsilon_r = 3.67$ and dielectric loss tangent $tg\delta = 0.03$ [9]. The input radiation is set as an incident Gaussian beam, determined by the lens L1b coupled with the calibrator. The reflectance, computed as the ratio of the Poynting vector fluxes of the scattered and incident radiation, is $R(120\,\text{GHz}) = 3.2 \cdot 10^{-6}$. The electric field amplitude within the cavity is reported in Fig.3-right.

The discrepancy in the results of the two approaches is mainly dictated by diffractive effects, which are neglected in the geometric approximation, and by the corresponding reflection coefficient used to derive the reflectance in the ray-tracing approach, which was measured at normal incidence in [8].

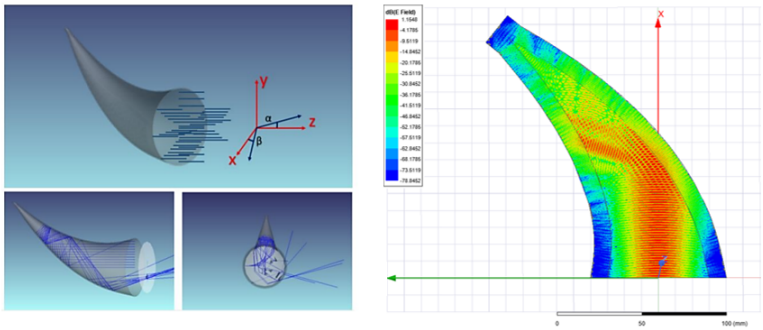

**Fig. 3** Left panel: light rays trajectories within the parabolic blackbody cavity from *ZEMAX-Optic Studio*. Right panel: *HFSS* simulation of the electic field amplitude propagating within a few wavelengths thick slice of the cavity at 120 GHz.

## 3 Performance Forecast

The performance of the instrument is assessed via ILC (Internal Linear Combination) based simulations. ILC methods exploit multi-frequency input maps to separate the map of the signal of interest from other components emitting in a sky region, exploiting the knowledge of their spectral shape. A constrained-ILC (c-ILC) [10] is applied to simulated sky maps, given by the superposition of the PySM [11] realizations of CMB anisotropies and thermal dust emission, as the main galactic foreground. The distortion map is added as an isotropic Compton-y map with $y = 1.77 \cdot 10^{-6}$, converted in brightness units Jy/sr. The input multi-frequency maps, with a spectral resolution $\Delta\nu = 10$ GHz, are absolutely-calibrated maps, with a map resolution parameter $N_{side} = 64$. Noise realizations are added as Gaussian noise, dominated by the photon noise from the cryostat window emission, taken as a grey-body with 1% emissivity and at 220 K, and by the atmospheric emission, based on the *a.m.* software [12] with precipitable-water-vapor PWV=0.15 mm. The measurements will be taken at fixed elevation of the cryostat axis. This, combined with the sky modulation from the spinning wedge mirror, results in the observation of 11 independent sky patches, as in Fig.4-left. Assuming 1 year of observations with $\eta = 30\%$ time-efficiency, the corresponding error per 1 deg$^2$ pixel and per spectral bin is evaluated from [13] as 110 Jy/sr and 323 Jy/sr, for the 150 and 220 GHz bands respectively. We assume a perfect atmospheric emission removal by the fast sky-dips procedure.

In the c-ILC machinery different orders of the thermal dust emission moment expansion are subtracted from the solution as in [14], to limit biases produced by the superposition of multiple dust populations and effects of average within the instrumental beam, which would produce unwanted distortion signals. The c-ILC $y$ solution maps of the first patch are reported in Fig.4-middle, where the $0^{th}$ order of the thermal dust emission and of CMB anisotropies are subtracted in the middle-top map, while up to the first derivative of the thermal dust emission is subtracted in the middle-bottom map. The second

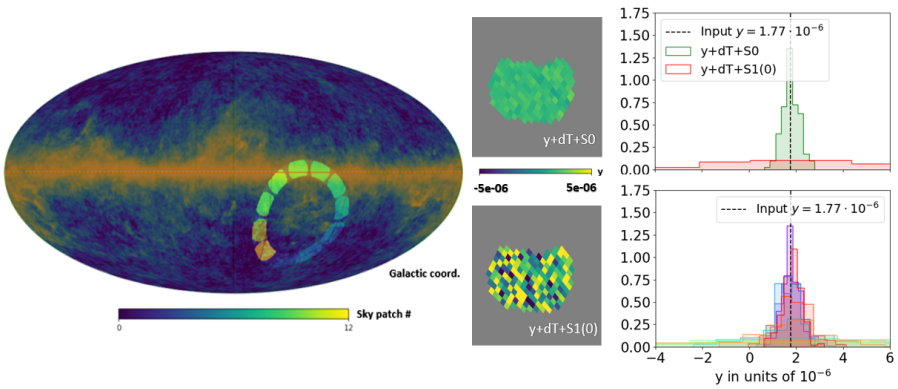


**Fig. 4** Left: COSMO coverage map superimposed over the 270 GHz thermal dust PySM map. Middle: output $y$ map of the sky patch # 1 from the c-ILC solution where the $0^{th}$ order of the thermal dust emission and the CMB anisotropies are removed from the solution (top) and where up to the $1^{st}$ order momentum of the thermal dust emission (bottom) are removed. Right: Histograms of the $y$ maps from different c-ILC solutions for the sky patch # 1 (top) and from the best c-ILC solutions over the 11 sky patches.

solution shows a variance degradation of the map as the higher orders of dust emission are subtracted. Histograms of the output Compton-y maps, reported in Fig.4 top-right for the sky patch # 1, also show that the best c-ILC solution is provided by the first solution. A weighted average of the independent $y$ distortion estimates over the 11 sky patches, evaluated from the histograms in Fig.4 bottom-right from the best c-ILC solutions, shows that COSMO can extract the isotropic comptonization parameter as $|y| = (1.79 \pm 0.19) \cdot 10^{-6}$.

The efficiency of the method is related to the noise level and the available frequency coverage, which are both limited and prevent the efficient removal of higher orders of the thermal dust emission for a ground-based implementation.

## 4 Conclusions

We presented preliminary simulations of the blackbody reference signal for CMB $y$-distortion measurements. We developed a blackbody cavity whose geometry maximises the absorption of input radiation and limits the effect of diffraction. *HFSS* simulations forecast a residual reflectance $R = 3.2 \cdot 10^{-6}$ at 120 GHz, corresponding to an emissivity $\epsilon \simeq 0.999999$, limiting the spurious distortion signal. We assessed the performance of COSMO via ILC-based simulations, showing that the isotropic comptonization parameter is extracted as $|y| = (1.79 \pm 0.19) \cdot 10^{-6}$ in the presence of foreground thermal dust emission and CMB anisotropies, assuming a perfect atmospheric emission removal and a noise realization dominated by the photon noise from the atmosphere and the cryostat window.

## References


1. J. Chluba, A. Kogut, S. P. Patil, M. H. Abitbol, N. Aghanim, Y. Ali-Haimoud, M. A. Amin, J. Aumont, N. Bartolo, K. Basu, E. S. Battistelli, R. Battye, D. Baumann, I. Ben-Dayan, B. Bolliet, J. R. Bond, F. R. Bouchet, C. P. Burgess, C. Burigana, C. T. Byrnes, G. Cabass, D. T. Chuss, S. Clesse, P. S. Cole, L. Dai, P. de Bernardis, J. Delabrouille, V. Desjacques, G. de Zotti, J. A. D. Diacoumis, E. Dimastrogiovanni, E. Di Valentino, J. Dunkley, R. Durrer, C. Dvorkin, J. Ellis, H. K. Eriksen, M. Fasiello, D. Fixsen, F. Finelli, R. Flauger, S. Galli, J. Garcia-Bellido, M. Gervasi, V. Gluscevic, D. Grin, L. Hart, C. Hernandez-Monteagudo, J. C. Hill, D. Jeong, B. R. Johnson, G. Lagache, E. Lee, A. Lewis, M. Liguori, M. Kamionkowski, R. Khatri, K. Kohri, E. Komatsu, K. E. Kunze, A. Mangilli, S. Masi, J. Mather, S. Matarrese, M. A. Miville-Deschenes, T. Montaruli, M. Munchmeyer, S. Mukherjee, T. Nakama, F. Nati, A. Ota, L. A. Page, E. Pajer, V. Poulin, A. Ravenni, C. Reichardt, M. Remazeilles, A. Rotti, J. A. Rubino-Martin, A. Sarkar, S. Sarkar, G. Savini, D. Scott, P. D. Serpico, J. Silk, T. Souradeep, D. N. Spergel, A. A. Starobinsky, R. Subrahmanyan, R. A. Sunyaev, E. Switzer, A. Tartari, H. Tashiro, R. Basu Thakur, T. Trombetti, B. Wallisch, B. D. Wandelt, I. K. Wehus, E.J. Wollack, M. Zaldarriaga, M. Zannoni. Astro2020 Science White Paper (2019). arXiv:1903.04218
2. D. J. Fixsen and J. C. Mather *ApJ* **581** 817 (2002). http://dx.doi.org/10.1086/344402
3. M. Gervasi, M. Zannoni, A. Tartari , G. Boella and G. Sironi *ApJ*, **688** 24 (2008). http://dx.doi.org/10.1086/592134.
4. G. D'Alessandro, P. de Bernardis, S. Masi, and A. Schillaci, *Appl. Opt.* **54**, 9269-9276 (2015). https://doi.org/10.1364/AO.54.009269
5. Tremblin P., Minier V., Schneider N., Durand G. Al., Ashley M. C. B., Lawrence J. S., Luong-van D. M., Storey J. W. V., Durand G. An., Reinert Y., Veyssiere C., Walter C., Ade P.,Calisse P. G., Challita Z., Fossat E., Sabbatini L., Pellegrini A., Ricaud P., Urban J. *A & A*, **535** (2011). DOI: 10.1051/0004-6361/201117345
6. D. K. Lambert and P. L. Richards, *Appl. Opt.* **17**, 1595-1602 (1978). https://doi.org/10.1364/AO.17.001595
7. H. Hemmati, J. C. Mather, and W. L. Eichhorn *Appl. Opt.* **24** 4489-4492 (1985). https://doi.org/10.1364/AO.24.004489
8. J. C. Mather, D. J. Fixsen, R. A. Shafer , C. Mosier and D. T. Wilkinson , *ApJ*,**512**, 511–520 (1999). DOI:10.1086/306805
9. J.W. Lamb *Int. J. Infrared Milli. Waves* **17** 1997–2034 (1996). https://doi.org/10.1007/BF02069487
10. M. Remazeilles, J. Delabrouille, J.-F. Cardoso *Monthly Notices of the Royal Astronomical Society*, **410**, 4 (2011). https://doi.org/10.1111/j.1365-2966.2010.17624.x
11. B. Thorne, J. Dunkley, D. Alonso, S. Naess, *Monthly Notices of the Royal Astronomical Society*, **469**, 2821–2833 (2017). https://doi.org/10.1093/mnras/stx949
12. S. Paine, The am atmospheric model (2019). https://doi.org/10.5281/zenodo.640645
13. P. de Bernardis, S. Colafrancesco, G. D'Alessandro, L. Lamagna, P. Marchegiani, S. Masi and A. Schillaci, *A&A*, **538** (2012). https://doi.org/10.1051/0004-6361/201118062
14. A. Rotti and J. Chluba *Monthly Notices of the Royal Astronomical Society*, **500**, 1 (2021). https://doi.org/10.1093/mnras/staa3292